

---

# MORPHOLOGICALLY TUNABLE MYCELIUM CHIPS FOR PHYSICAL RESERVOIR COMPUTING

---

**Orkan Telhan\***

Ecovative

Green Island, NY 12183

[orkan@design.bio](mailto:orkan@design.bio)

**Jake Winiski**

Ecovative

Green Island, NY 12183

[jake@ecovative.com](mailto:jake@ecovative.com)

**Damen Schaak**

Ecovative

Green Island, NY 12183

[damen@ecovative.com](mailto:damen@ecovative.com)

**Mike Siegel**

Ecovative

Green Island, NY 12183

[mike@ecovative.com](mailto:mike@ecovative.com)

**Neale Petrillo**

Ecovative

Green Island, NY 12183

[neale@ecovative.com](mailto:neale@ecovative.com)

**Eben Bayer**

Ecovative

Green Island, NY 12183

[eben@ecovative.com](mailto:eben@ecovative.com)

August 4, 2025

## ABSTRACT

We introduce a neuromorphic computing substrate based on PEDOT:PSS-infused mycelium, a biofabricated, morphologically tunable material that can be engineered into electrically active components including resistors, capacitors, and non-linear elements. Leveraging the principles of physical reservoir computing, we demonstrate that hyphal networks grown under controlled environmental conditions can transform time-varying inputs into nonlinear, high-dimensional state trajectories, enabling machine learning tasks such as NARMA-10 sequence prediction. The chips are produced using a “design-grow-compute” workflow that integrates morphological modeling, parametric growth protocols, and vacuum-assisted polymer infusion. Morphological complexity is shown to influence charge transport and memory capacity, offering a new axis of control for designing analog computational architectures. Our prototype chips included up to 16 spatially distinct reservoirs that interface with a custom carrier board enabling analog signal conditioning and readout. Benchmarking revealed robust nonlinearity, temporal dynamics, and task-relevant separability. Unlike memristor arrays, photonic, or living-cell-based reservoir systems, our non-living analog mycelium chip is low-cost, biodegradable, and scalable using existing mushroom farming infrastructure, with production yields exceeding 3 million chips per growth cycle. This work advances a novel direction for biologically derived, single-use (compostable) or very large-scale machine learning hardware and introduces mycelium as a functional medium for analog inference.

## 1 Introduction

Physical reservoir computing is a framework that uses the noisy, transient, and non-linear aspects of physical systems to compute information [1, 2]. Its underlying premise is to use a network of dynamic reservoirs to process low-dimensional data into high dimensions and focus the training into a single readout layer. Historically, it is demonstrated that reservoir computing offers significant advantages in ML and AI applications [3, 4]. Unlike neural networks, in which the weights of each layer must be updated, reservoir computing requires only one layer to be trained, which eliminates both the computational cost for backpropagation and the need for GPUs for matrix manipulations. As the readout layer can be implemented in traditional CPUs, reservoirs must be efficient, versatile, low-power, and highly tunable. Reservoir

---

\*Corresponding author: [orkan@design.bio](mailto:orkan@design.bio)

systems can be trained with smaller datasets, fewer parameters and be suitable for online and continuous learning applications.

Physical reservoirs can range from photonic circuits to soft robotics, memristors, spintronic devices, which offer novel ways to process time-varying inputs into rich internal dynamics that encode temporal patterns, enabling tasks like signal classification, prediction, and control [5, 6, 7]. Such reservoirs promise a low-power, low-latency and continuous machine learning paradigm that can leverage the mechanical or thermodynamic properties of material systems [8]. Reservoir computers offer unconventional computing architectures that can be massively scaled or parallelized in different embodiments. The computational elements can be soft or rigid co-located or de-centralized [9].

While a variety of physical systems are evaluated as reservoir computers, not every physical non-linear system makes a good reservoir [10]. For example, a physical system should be able to give the same response when the same input is repeated [11]. The memory capacity (MC) of a reservoir also defines its ability to predict the same signal with different amounts of delay. Higher memory capacity indicates the system can retain and distinguish longer sequences of past input, making it better suited for time-dependent tasks like speech recognition, system identification, or time series forecasting.

Different physical reservoir designs which use biological, optical, electrical, magnetic, and mechanical components require different levels of manufacturing complexity and pose unique challenges for scalability. For example within the domain of Electrical RC, different memristor architectures provide non-linearity through modulating conductivity over analog resistive elements [12, 13, 14]. The memristor-based memory market has already reportedly reached \$419 million in 2023, but challenges in achieving yield, reliability, device-level precision (high-level fixed point arithmetic) and high compute density currently slow down accelerating their use in-memory computing applications [15]. Memristor reservoir technology requires further development, and remains insufficiently mature for practical deployment as a replacement to conventional machine-learning infrastructure [16].

Mycelium, the vegetative structure of fungi, offers a novel and scalable medium for neuromorphic reservoir computing. Reservoir chips can be grown at existing mushroom farms without capital-intensive infrastructure or specialized tooling. In this paper, we demonstrate custom mycelium reservoir morphologies with tunable electrical properties—such as resistance, capacitance, and decay rate—designed pre-growth using a predictive model. We tested the feasibility of a model-driven “design-grow-compute” framework to grow mycelium chips using high-throughput benchtop reactors, which thermodynamically simulate the conditions in large scale farms.

The chips were grown in 19×14×4cm trays, cut to the desired dimensions, and vacuum-infused with PEDOT:PSS, a conductive polymer widely used in the thin-film industry [17]. We have benchmarked different chip morphologies and evaluated their potential as reservoirs by assessing their separability, memory capacity, nonlinearity, and task accuracy. We quantified differences in morphological complexity and conductive dynamics as they transform incoming signals and conceptualize this transformation as a form of kernelization—a temporal, analog, nonlinear feature expansion. In this framework, a mycelium reservoir functions as a physical kernel, projecting input signals into a dynamic, high-dimensional feature space in which a simple readout can perform complex tasks such as classification [18].

When a physical kernel transforms an incoming signal via complex nonlinear dynamics, it implicitly maps that signal into a higher-dimensional space—without the need for symbolic or numerical encoding. In the context of mycelium reservoirs, the “kernel function” is physically instantiated through the organism’s morphology and conductive behavior. To design or tune such a kernel, we use a growth model that adapts the physical structure of the reservoir to suit a given computational task. Alternatively, the state of the kernel can be modulated by external stimuli such as temperature or electrical conductivity—though such dynamic tuning is beyond the scope of this paper.

Mycelium chips were fabricated with 16 spatially distinct reservoirs and mounted on a custom-designed carrier board that supports signal amplification, summation, and voltage level translation for analog interfacing (Figure 1). Each reservoir is electrically addressable, enabling parallel or sequential activation for diverse machine learning tasks. The modular architecture allows individual chips to be used independently or stacked to form larger, multi-reservoir computing arrays. While the intrinsic conductive properties of individual reservoirs are fixed post-fabrication, a form of functional learning can be implemented by dynamically routing input signals through subsets of reservoirs with predictable nonlinear responses. Using a multiplexing scheme, the system can reconfigure information flow toward nodes exhibiting desirable characteristics—such as sharp current transitions driven by space-charge-limited conduction (SCLC) [19, 20]. By exploiting these diode-like behaviors and known voltage-response boundaries, the network can be tuned to enhance task-specific performance without altering material weights, enabling adaptive computation through structural reconfiguration rather than parameter updates.

To evaluate the computational capabilities of the mycelium-based reservoirs, we conducted a series of benchmark tests focused on temporal memory, nonlinearity, and sequence modeling. These included impulse response and correlation-based memory assessments, settling time characterization, and the NARMA-10 benchmark—an established

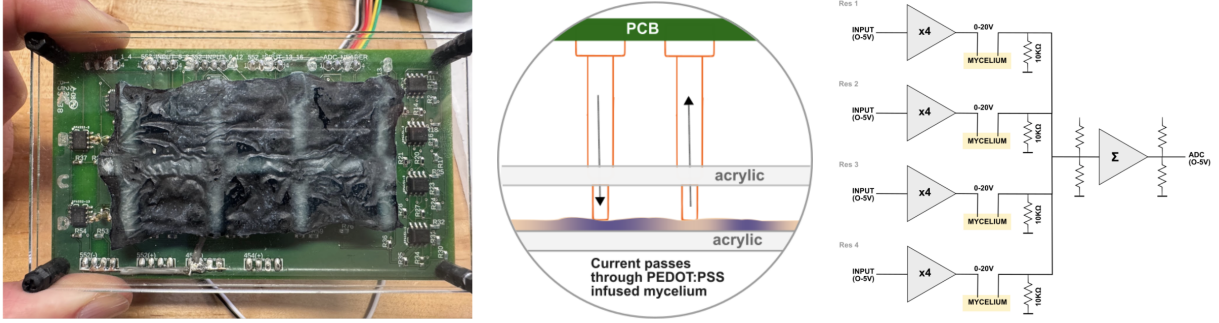


Figure 1: Neuromorphic Mycelium Chip mounted on a carrier board, which dispatches signals to 16 reservoirs. 4 sets of 4 reservoirs are summed with a summing amplifier and conditioned for ADC. A grid of pogo pins define locations of reservoirs, from which electrical signals are passed through mycelium.

nonlinear autoregressive task used to evaluate temporal information processing in physical reservoirs [6]. Mycelium reservoirs exhibited significant autocorrelation, cross-correlation, and nonlinear voltage responses consistent with memory-rich dynamics. When evaluated using regression models such as ridge regression and random forest, the reservoirs demonstrated predictive capability across delayed inputs, confirming their suitability for temporal inference tasks.

Our design required mycelium chips to be sandwiched between acrylic plates, and then mounted on a carrier PCB where digital or analog signals can be interfaced with the reservoir. This form factor allows multiple chips to be stacked and used for multiple machine learning tasks in parallel. In our experiments, the chips were not treated with any additional chemistry –shelf-stabilized using coatings or sealants. As an initial application area, we considered their applications in single-use or disposable electronics such as point-of-care diagnostics, food spoilage or hazard detection, and physical cryptography—where their tamper-proof construction and biodegradable composition ensure they are fully compostable within three months [21, 22, 23, 24]. Morphological tuning paired with post-growth infusion allows us to parametrically set the response intervals of the reservoirs, and even pave the path towards building multi-stage neural-network-like inference engines with set weights. In practical contexts such as packaging or environmental monitoring, these chips can be triggered by spoilage events (e.g., gas release or pH shift), classify contamination type and severity using embedded analog inference, and activate localized responses such as color change or signal dispatch. Mycelium chips can potentially be sealed against moisture loss or reinforced for durability with traditional tanning chemistry, enabling both extended field use and safe, compostable disposal.

Mycelium has been explored for its computational potential both as a living organism and as a material [25]. Adamatsky et al. demonstrated that live hyphal tissue can transmit signals through substrate and be used to build digital gates [26, 27]. Hyphal cells can also retain moisture and electrolytes in their network and store a reasonable amount of charge [28, 29, 30].

Flexible or rigid mycelium sheets also function as carrier surfaces to carry conductive traces and offer a biodegradable alternative to printed circuit boards (PCBs) [31]. Mycelium can be coated with copper using physical vapor deposition or electroplated with gold to achieve highly conductive traces ( $> 9 \times 10^4 \text{ S cm}^{-1}$ ). Danninger also demonstrated that mycelium can be soaked with PEDOT:PSS to create vias that would allow multiple layers to be electrically bridged to create stackable circuits.

Filamentous fungi display remarkable phenotypic plasticity, dynamically remodeling their mycelial networks in response to spatial and environmental cues such as nutrient gradients and physical heterogeneity [32]. This plasticity is manifested through context-dependent modulation of branching, fusion, and growth direction, enabling decentralized adaptation for efficient resource acquisition, structural resilience, and morphological optimization. Morphological engineering in filamentous fungi in submerged culture systems involves the deliberate manipulation of growth form to enhance fermentation performance, leveraging the inherent phenotypic plasticity of these organisms [33].

Aerial mycelium refers to a cohesive, vegetative network of fungal hyphae that grows into open space above a nutritive substrate under solid-state conditions, forming a pure mycelial material without the development of fruiting bodies [34]. We morphologically engineered aerial mycelium by leveraging environmental strategies to control growth topology and tissue density. Specifically, we used topology adjustment layers—structured, perforated surfaces placed above the substrate—to regulate localized gas exchange and humidity, guiding hyphal emergence into geometrically defined

patterns ranging from homogeneous to heterogeneous [35, 36]. The configuration of the growth chamber, including wall height and the application of casing layers, influenced internal gradients of CO<sub>2</sub> and humidity, enabling directional control over vertical expansion and spatial uniformity [37]. Together, these methods enable scalable and repeatable engineering of mycelial structure.

## 2 Methods

### 2.1 Mycelium Production

Pure mycelium mats were produced according to Ecovative's aerial mycelium platform using a benchtop bioreactor system, which under varying growth conditions, yielded a variety of intra- and inter-mat tissue morphologies. This platform leverages the natural plasticity of vegetative growth to engineer a wide morphological vocabulary, allowing for targeted variation in both organizational complexity and density within a single cohesive mycelial thallus. Within the scope of these studies, this provided a population of aerial mycelium mats from which various morphological classes of material could be selected. All mycelium mats were produced with Ecovative's core foam strain and oven dried to < 10% moisture content prior to use, with stock panels up to 70mm in thickness (z-dimension) with arbitrary dimensionality in the x- and y-dimensions.

### 2.2 Mycelium Chip Specimen Preparation

Stock mycelium mats were sliced in the x-y plane using a commercial deli slicer to 1mm thickness, then further cut to 50x100mm in the x-y dimensions. The specimen was then misted with 70% isopropanol as a pre-wetting step and immediately floated in an excess of 1.3% stock solution of PEDOT:PSS (Ossila) in a reservoir plate (Corning HTS Transwell CLS4395). Specimens were then vacuum infused at -0.8 bar for 30 seconds (Vevor 5 gallon vacuum chamber with 3.5 CFM pump). After vacuum infusion specimens were removed from the reservoir plate and blotted with a paper towel to remove excess PEDOT:PSS.

Specimens were sandwiched between two sheets of acrylic and dried to 10% moisture content in a commercial dehydrator at 24C overnight. The ridges of the enclosure allowed PEDOT to be localized into a grid pattern as the pressure applied by the acrylic forced the polymer into non-pressurized areas.

### 2.3 Mycelium Chip Specimen Imaging and Morphological Featurization

All 50x100x1mm mycelium specimens were imaged under transmitted light using the film scanning function of an Epson V600 scanner, both before and after PEDOT:PSS infusion.

Morphological analysis was conducted via a custom Python pipeline using OpenCV and SciPy. High-resolution images were converted to grayscale, contrast-enhanced, and smoothed with Gaussian blur to improve feature clarity. Blob detection was performed using parameterized filters for area, circularity, convexity, and inertia, enabling quantification of individual morphological units. For each blob, diameter, area, and mean grayscale intensity were extracted, with summary statistics (mean, standard deviation, min, max, median) computed. Whole-image texture features were also derived from grayscale histograms, including contrast, energy, homogeneity, entropy, variance, skewness, kurtosis, autocorrelation, and difference entropy. This feature set captured both blob-level and global image characteristics for subsequent dimension reduction and correlation with electrical properties.

### 2.4 Mycelium Chip Electrical Characterization

For each specimen, resistance, capacitance, and voltage–current (I–V) curves were measured. Resistance was recorded in a matrix pattern using a Keithley 2400 source meter with 4-wire Keithley 5805 Kelvin probes at 2V, 16V, and 18V. Capacitance was measured at the same locations using an ET4410 LCR meter with a 1KHz sine wave (1V peak-to-peak, 100Ω input impedance). I–V curves were acquired using a Keithley 2400 with a full voltage sweep from 1–20V in 0.5V steps (Figure 2). All tests were repeated to ensure reproducibility, consistently revealing non-linear I–V behavior.

To calibrate each chip, electrical response was evaluated at eight locations by passing a 0–20V test signal through gold-plated prongs (3mm apart), arranged in a matrix, and recording voltage decay time.

## 2.5 Classification of Local Electrical Properties of Mycelium Chip Specimens as a Function of Global and Local Morphological Qualities

To identify distinct mycelium morphologies, aerial mycelium samples were processed through a morphological featurization pipeline, followed by PCA for dimensionality reduction and visualization, and k-means clustering for discrete group identification. Features were standardized using z-score normalization prior to clustering. The optimal number of clusters was determined via the elbow method (minimizing WCSS). From the resulting clusters, three were selected to maximize morphological diversity by choosing the pair with the greatest centroid distance and a third with the largest combined distance from the first two (See Supplementary Document Section 1.4).

Clusters 0, 2, and 3 were selected, and one representative specimen from each was prepared as chip specimens in acrylic templates for localized morphological and electrical evaluation at 9 defined positions.

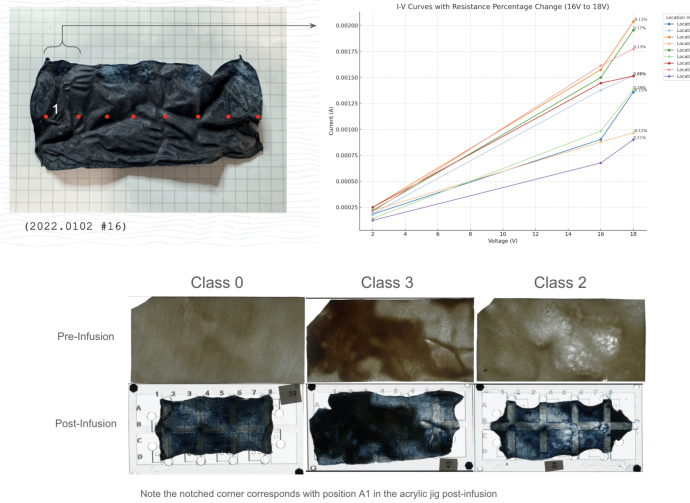


Figure 2: (Top) Electrical characterization reveals consistent non-linear I–V behavior across specimens via resistance, capacitance, and voltage sweep measurements. (Below) Representative chip specimens from clusters 0, 2, and 3, pre- and post-PEDOT:PSS infusion.

Specimens were imaged before and after PEDOT:PSS infusion, cropped to final dimensions, and aligned using rigid body transformation in FIJI [38]. ROIs were defined from the post-infusion template and applied to the pre-infusion image to correlate electrical data with native morphology. Histogram-based image features (e.g., mean, skewness, entropy, contrast) were extracted per ROI, and whole-chip morphology was dimension reduced via PCA. Electrical data were processed by fitting linear models to IV curves and extracting slope, intercept,  $R^2$ , and residuals. Skewed targets were transformed (Box-Cox/log) for model training (Figure 3).

PCA on electrical features revealed high covariability, with PC1 accounting for over 90% of variance. Mutual information analysis ranked predictive features, revealing strongest relationships with global morphology (density, complexity), followed by local density, texture, and eccentricity (Figure 4).

A feedforward neural network was trained to predict PC1 from global and local features using LOOCV. The architecture used two hidden layers (128, 64 ReLU units), L2 regularization, and dropout. The model achieved  $R^2 = 0.74$ , indicating strong predictive ability (See supplemental information Fig. S14). To validate the systematic nature of morphology-property relationships, spatial autocorrelation analysis using Moran's I confirmed significant organization of electrical resistance within the morphological feature space ( $p = 0.003\text{--}0.007$  across test positions). SHAP analysis revealed morphological complexity and density (PC1 and PC2) as the strongest predictors of electrical resistance, exceeding the influence of PEDOT:PSS uptake (Supplemental Fig. S15). This hierarchy confirms that electrical properties are sensitive to morphological variation, and thus may be designed through morphological engineering independent of polymer characteristics, with structural complexity and density serving as the primary control parameters.

These results confirm that native mycelial morphology is highly predictive of post-infusion electrical behavior independent of the absolute mass uptake of PEDOT:PSS. This enables pre-infusion classification of electrical properties across a mycelium sheet, allowing for informed region selection to optimize reservoir computing function. By predicting

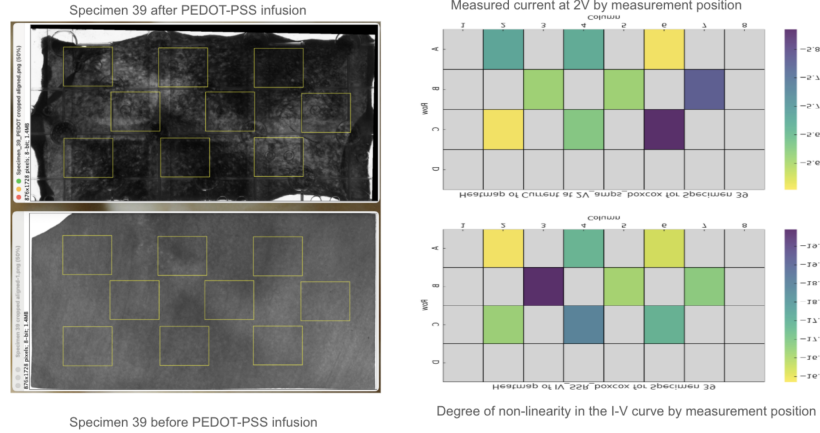


Figure 3: ROI alignment and mapped electrical features (class 0 specimen) showing spatial variation in current and I–V non-linearity.

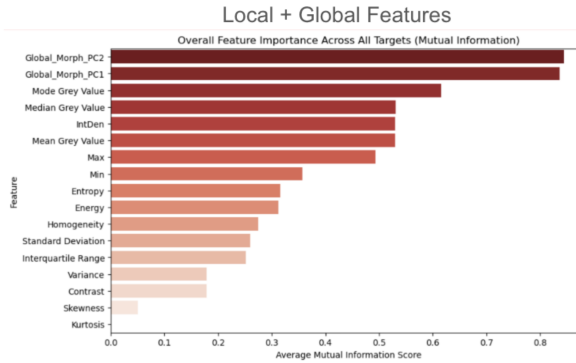


Figure 4: Mutual information highlights global and local morphological features of electrical behavior (PC1 and PC2 are global, all others are local)

electrical response from morphology, this approach supports rational design and reduced empirical trial-and-error in substrate engineering.

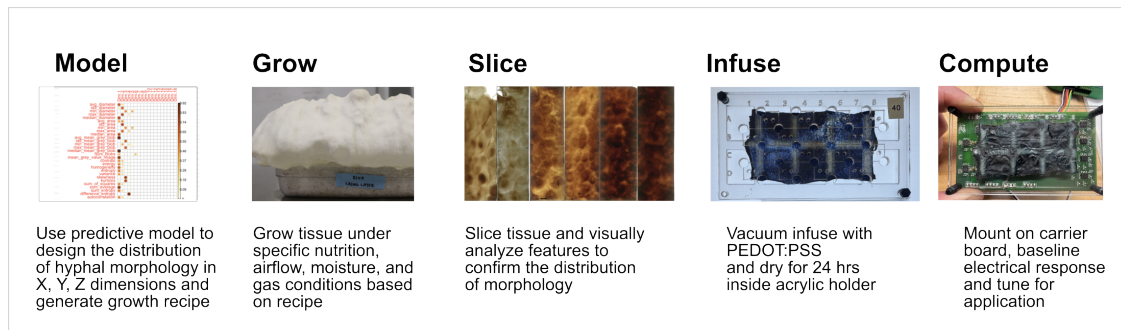


Figure 5: Full-stack workflow for producing application-specific mycelium chips (ASMCs), from in silico design through modeling, growth, slicing, infusion, electrical calibration, and computation steps.

## 2.6 Design - Grow - Compute Workflow

Our approach enables a full-stack workflow for developing application-specific mycelium chips (ASMCs) that are designed in silico, biologically grown, post-processed, and directly interfaced with electronic systems (Figure 5). The process begins with feature selection, such as the number, spatial distribution, and electrical characteristics (e.g., resistance, capacitance) of reservoirs, guided by parameters derived from both global and local morphological feature spaces. These desired traits are translated into environmental growth parameters specific to the production setup (e.g., half-tray, full-tray, or bed-scale bioreactors). Mycelium tissue is typically grown in one- or two-week cycles, with multiple chip designs cultivated in parallel. After harvest, tissues are dried, precision-sliced, and imaged. These pre-infusion images are analyzed to extract morphological features and feed back into predictive models for iterative design refinement. Sliced specimens are mounted into acrylic cartridges and infused with PEDOT:PSS, as described in the Methods section; each cartridge is referred to as a single chip. Chips are then mounted onto carrier boards for electrical characterization. A calibration routine pulses each reservoir at various voltage levels to baseline its dynamic response characteristics, preparing the chip for deployment in analog computing tasks.

## 3 Results

### 3.1 Computing with Neuromorphic Mycelium

We designed the carrier board that serves as an analog interface to the reservoir network, routing both input signals and their corresponding collection pathways. Sixteen independent input channels operate in parallel, enabling the configuration of reservoirs independently [39]. Additionally, multiple channels can be used sequentially to define reservoir sub-clusters composed of several inputs. The outputs from four channels are summed via a non-inverting operational amplifier, which also conditions the signals for acquisition by an analog-to-digital converter (ADC). Multiple carrier boards can be networked together to construct more complex reservoir layouts.

The input to the mycelium chip can be digital—from the output of a microcontroller, or analog—a waveform/signal directly sourced from a sensor. For our prototypes we used Digilent’s Analog Discovery 2 and 3 devices with both continuous and discrete input to test the capabilities of the reservoirs. The carrier board offers a two stage amplification process. Each signal from 0-5V range is amplified with a non-inverting amplifier with 4x gain to achieve the critical 16-18V threshold that causes the non-linear jump in current flow. After the summation phase, the signals are stepped down with a voltage divider back to 0-5V range and buffered for the ADC.

We have evaluated the chip’s computational capabilities on two fronts: memory response and temporal processing capacity. Our experimental setup used the analog carrier chip that received input from one Analog Discovery 2 (channels 1&2) and one Analog Discovery 3 Device (channels 1). The summed output of three channels were read into the Analog Discovery 3 device. We used 3 reservoirs—locations A1, A4, and A6 on 3 chips on the same task.

### 3.2 Memory Response

We evaluated the mycelium reservoir’s temporal dynamics by applying three input types—random pulses, step signals, and sine waves—with programmable delays (Table 1). These patterns were selected to probe distinct memory regimes across three reservoirs in one chip. Pearson autocorrelation and cross-correlation metrics quantified how the reservoir state evolved over time in response to input.

Under step input, the reservoir exhibited strong memory, with autocorrelation peaking at 0.85 (lag=6s) and cross-correlation reaching 1.0 at zero lag, indicating both persistence and immediate input-state coupling. Ridge regression using only the current input yielded an  $R^2 = 0.74$ , which did not improve with historical input, suggesting that system dynamics were saturated or dominated by present-state behavior. To quantify temporal resolution, we measured settling time—the interval for voltage to return to 90% of baseline after a step input. Settling time varied across input types, with step inputs requiring up to 600ms to stabilize (Table 1), while responses to stochastic or periodic signals appeared faster or continuous. We therefore adopted a conservative sub-second sampling interval for memory evaluations to accommodate this variability.

With random input (1.1–3.49V), autocorrelation was lower (0.20 at 0.3s lag), while cross-correlation remained high (1.0 at lag 0), reflecting strong immediate response with limited carryover. Incorporating signal history modestly improved regression accuracy ( $R^2$  increasing from 0.577 to 0.611), indicating shallow memory under stochastic conditions. For sine wave input (1.2–3.5V), autocorrelation and cross-correlation peaked at 0.497 and 0.689, respectively, both at 1s lag—aligned with the signal’s periodicity (Fig 7). Here,  $R^2$  increased from 0.4745 to 0.5005 with history, confirming the system’s capacity to track structured temporal inputs.

Table 1: Temporal dynamics characterization across input types, revealing memory retention and response characteristics of mycelium reservoirs.

Input Type	Max Autocorr (lag)	Max Crosscorr (lag)	R <sup>2</sup> (Current)	R <sup>2</sup> (History)	R <sup>2</sup> Gain	Settling Time (s)
Step	0.85 (6s)	1.00 (0s)	0.740	0.740	0.000	0.6
Random	0.20 (0.3s)	1.00 (0s)	0.577	0.611	0.034	0.3
Sine	0.497 (1s)	0.689 (1s)	0.4745	0.5005	0.026	1.0

Collectively, these results show that the mycelium reservoir captures a spectrum of memory behaviors: stable and sustained under step input, transient under random signals, and phase-locked under periodic waveforms. This responsiveness supports its suitability for time-dependent analog computation.

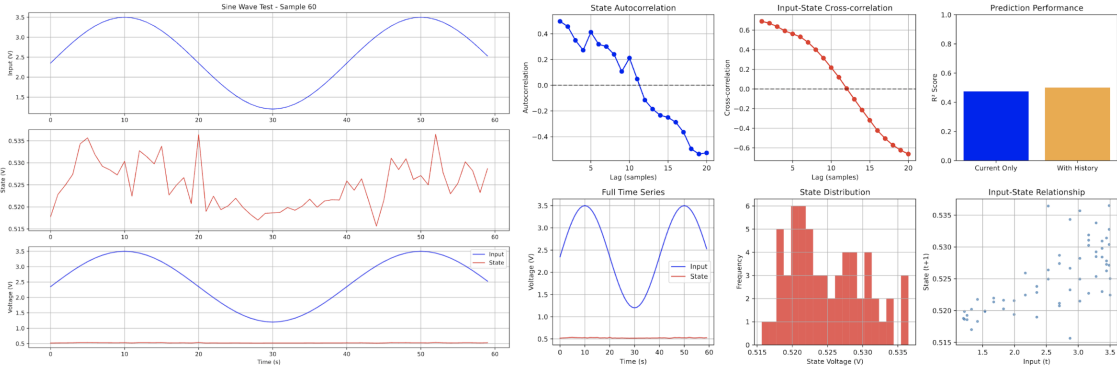


Figure 6: Sine wave input reveals phase-locked memory behavior, consistent with temporal encoding.

### 3.3 NARMA-10 Benchmark

To evaluate the reservoir’s temporal processing capacity, we employed the standard Nonlinear Auto-Regressive Moving Average task of order 10 (NARMA-10)—a widely used benchmark for assessing nonlinear memory in physical reservoir systems [6, 40]. This task requires the reservoir to predict the next value in a nonlinear time series based on the preceding 10 inputs, offering a stringent test of both memory depth and nonlinear transformation.

We used the same chip and the same three reservoirs for the test. We generated 1,000 training samples by applying voltage signals in the 0–5 V range to the mycelium reservoirs. Feature representations included the raw reservoir state, its square, and trigonometric expansions (e.g.,  $\sin(\text{state} \times 3)$ ,  $\cos(\text{state} \times 2)$ ). These enriched features were used to train both Ridge regression and Random Forest models to probe the substrate’s nonlinear encoding capacity and temporal dependencies. Tests were conducted across multiple reservoir configurations to assess system reliability.

Our mycelium reservoir system achieved NARMA-10 performance across three independent test experiments with Ridge regression yielding RMSE values of 0.102–0.106, corresponding to normalized root mean squared error (NRMSE) of 1.01–1.07. Here, NRMSE is computed as  $\text{NRMSE} = \frac{\text{RMSE}}{\sigma(\text{target})}$ , where  $\sigma(\text{target})$  denotes the standard deviation of the target values. Some literature may use alternative normalizations (e.g., by range), but this standard definition enables the most direct comparison with established reservoir computing benchmarks.

While this performance indicates functional temporal processing capability, it falls below the optimized performance of specialized electronic reservoir systems (NRMSE 0.056–0.410). However, this represents the first demonstration of temporal computing in a biodegradable, agriculturally scalable substrate.

The NARMA-10 evaluation across multiple independent trials revealed several important system characteristics: (1) consistent performance reproducibility (NRMSE range 1.01–1.07 across three experiments), demonstrating reliable temporal processing; (2) successful nonlinear feature extraction from mycelial network dynamics; (3) effective integration of morphologically-tuned electrical properties with computational tasks; and (4) stable operation within the identified 16–18 V nonlinear regime. Random Forest models showed comparable performance across trials, confirming the robustness of the underlying reservoir dynamics.

Our results establish that biological reservoir computing is achievable, with performance trade-offs justified by unique advantages not available in conventional approaches. The demonstrated NARMA-10 capability, while suboptimal compared to electronic systems, validates the core concept of mycelium-based neuromorphic computing and provides a foundation for morphological optimization strategies. Importantly, this performance is achieved at <\$1 per chip with complete biodegradability—representing orders of magnitude cost savings and the first sustainable reservoir computing platform.

The consistent performance across different readout models and the successful temporal processing demonstration support the viability of mycelium reservoirs for applications where sustainability, cost, and biological integration are prioritized over absolute computational performance. This work establishes a new paradigm for environmentally sustainable neuromorphic computing with clear pathways for performance enhancement through morphological engineering.

## 4 Discussion

### 4.1 Operational Range and Durability of Mycelium Chips

While conventional AI chips operate at sub-1V core voltages to minimize power consumption and thermal load [41], our analog mycelium-based reservoirs require signal amplification to 16–18V to activate non-linear conduction regimes. This elevated voltage reflects the intrinsic charge transport behavior of PEDOT:PSS within porous mycelial matrices, where trap-state saturation consistent with space-charge-limited conduction (SCLC) enables diode-like transitions essential for analog inference [42]. Though uncommon in CMOS-scale devices, such operational ranges are acceptable in low-power, passive systems, especially when intended for single-use or intermittent-use applications where energy consumption is limited and bio-compatibility, biodegradability, and cost are the dominant design constraints. The platform is also compatible with energy scavenging or capacitor-driven systems under field conditions.

Mycelium chips were evaluated in ambient conditions (22°C unpowered; 36°C during operation, due to carrier board heating). Across multiple cycles, voltage response curves showed modest drift, likely due to moisture exchange and morphological reconfiguration. No sealing or moisture-stabilizing treatment was applied to these prototypes, so gradual conductivity decline over time is expected. However, baseline recalibration, range re-mapping, and voltage correction factors allow compensation for mild aging effects. In over 50 tests per chip, performance remained stable and repeatable, suggesting practical durability within the intended use window.

### 4.2 Scalability Potential

Compared to other neuromorphic platforms, mycelium-based reservoirs offer a unique combination of biological integration, morphological tunability, and ultra-low fabrication cost. While memristor arrays provide superior performance with non-volatile dynamics at higher speeds, they require precision fabrication and face scaling challenges (Table 2). Photonic reservoirs offer excellent computational performance (NMSE 0.014–0.127) and unmatched bandwidth but remain difficult to fabricate and scale beyond lab prototypes.

Table 2: Performance and cost comparison of physical reservoir computing systems. Reported NRMSE values may differ by normalization method. Missing entries indicate unavailable or incomparable data. Cost and power estimates reflect material, fabrication, and operational differences across architectures.

System	Power Consumption	NARMA-10 NRMSE	Processing Speed	Scalability	Sustainability	Cost Estimate
<b>Mycelium Reservoir</b>	2.5–30mW	1.01–1.07 (this work)	0.1–1s settling	Agricultural scale	Biodegradable, compostable	<1/chip, ~50/carrier
<b>Memristor Arrays</b>	0.005mW@MHz [4] – 5nJ–4.28aJ [43]	0.00361 [4] – 0.036 [44]	MHz–GHz	Fab-limited	E-waste concern	\$500–5,000+
<b>Photonic RC</b>	5100mW [45]	0.0143 [45], 0.127 [46]	60GHz	Lab/specialty fab	Traditional materials	\$5,000–50,000+
<b>Ion-Gating RC</b>	Ultra-low power	0.00938 [47]	Not reported	Nanodevice scale	Traditional materials	\$1,000–10,000+
<b>Spin Wave RC</b>	14.2W@50Hz [48] 284μJ/input	0.168 [48]	50MHz (20ns response)	Research scale	Traditional materials	Non-commercial

Our mycelium reservoir system achieves functional NARMA-10 performance (NMSE 1.01-1.07) that, while suboptimal compared to electronic systems, demonstrates the first temporal computing in a biodegradable substrate. This performance is achieved at <\$1 per chip—a 500-50,000x cost advantage over competing technologies (\$500-50,000+)—while uniquely offering complete biodegradability and agricultural-scale manufacturing.

Unlike previous bio-inspired or living-biology reservoir computing approaches [49, 50, 51, 52], our work explores non-living mycelium as a highly scalable substrate. We demonstrated that electrical properties reflect morphological variation across chips  $R^2 = 0.74$ , with morphological development controllable through biomanufacturing parameters. This suggests that electrical properties influencing reservoir characteristics may be designed into mycelium chips during the biofabrication process independent of the inherent characteristics of PEDOT:PSS by targeted morphological engineering. Specific tissue density and organizational characteristics can be programmed by modifying environmental conditions during growth (Figure 7).

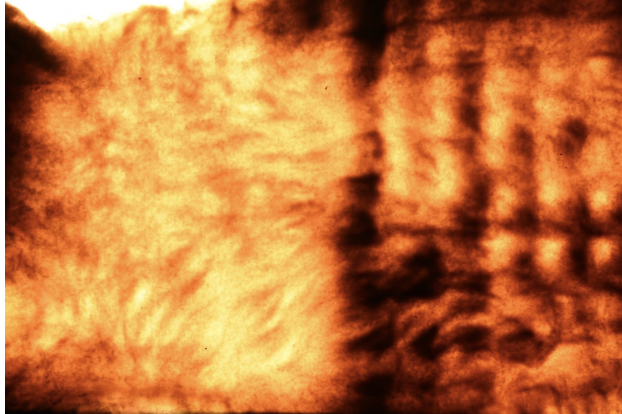


Figure 7: Various mycelium chip morphologies are mycofabricated within a single contiguous 8x12 inch sheet using aerial mycelium morphological engineering techniques (shown by transmitted light photography after slicing).

This work introduces a novel biomanufacturing paradigm for the first disposable ML inference chip. Aerial mycelium here functions simultaneously as substrate, signal processor, and morphological kernel. Analogous to panelized PCB manufacturing, a single aerial mycelium panel can embed diverse, task-specific morphologies in discrete regions. A standard Dutch-style mushroom bed ( $1.34 \times 40$  m) can produce over 3 million chips per 7-14 day cycle [53], enabling a fully integrated, biodegradable hardware stack for sustainable, task-specific inference where cost and environmental impact outweigh absolute computational performance. Building on recent demonstrations of conductive mycelium circuit substrates [31], we envision a future in which aerial mycelium serves as both substrate and computational medium, enabling a fully integrated, biodegradable hardware stack for sustainable, task-specific inference.

## Acknowledgments

This research was developed with funding from the Defense Advanced Research Projects Agency (DARPA). The views, opinions, and/or findings expressed are those of the author(s) and should not be interpreted as representing the official views or policies of the Department of Defense or the U.S. Government.

## Data Availability

The datasets generated and analyzed during the current study are available from the corresponding author upon reasonable request.

## Code Availability

All code used for signal processing and reservoir evaluation is available at <https://github.com/otelhan/NeuromorphicMyceliumChip>

## Supplementary Information

See Appendix below for additional figures and method discussion.

## References

- [1] Kohei Nakajima. Physical reservoir computing—an introductory perspective. *Japanese Journal of Applied Physics*, 59(6):060501, 2020.
- [2] Matteo Cucchi, Samuel Abreu, Giuseppe Ciccone, Daniel Brunner, and Hans Kleemann. Hands-on reservoir computing: a tutorial for practical implementation. *Neuromorphic Computing and Engineering*, 2(3):032002, 2022.
- [3] Xiangpeng Liang, Jianshi Tang, Yinan Zhong, et al. Physical reservoir computing with emerging electronics. *Nature Electronics*, 7:193–206, 2024.
- [4] Can Du, Fuxi Cai, Mohammed A Zidan, Wen Ma, Sae Hyeok Lee, and Wei D Lu. Reservoir computing using dynamic memristors for temporal information processing. *Nature Communications*, 8(1):2204, 2017.
- [5] Carver Mead. Neuromorphic electronic systems. *Proceedings of the IEEE*, 78(10):1629–1636, 2002.
- [6] Gouhei Tanaka, Toshiyuki Yamane, Jean Benoit Héroux, Ryosho Nakane, Naoki Kanazawa, Seiji Takeda, Hidetoshi Numata, Daiju Nakano, and Akira Hirose. Recent advances in physical reservoir computing: A review. *Neural Networks*, 115:100–123, 2019.
- [7] Danijela Marković, Alice Mizrahi, Damien Querlioz, and Julie Grollier. Physics for neuromorphic computing. *Nature Reviews Physics*, 2(9):499–510, 2020.
- [8] Alireza Goudarzi, Peter Banda, Matthew R Lakin, Christof Teuscher, and Darko Stefanovic. A comparative study of reservoir computing for temporal signal processing. *arXiv preprint arXiv:1401.2224*, 2014.
- [9] Dhireesha Kudithipudi, Catherine Schuman, Craig M Vineyard, Tarun Pandit, Cory Merkel, Rajkumar Kubendran, James B Aimone, Garrick Orchard, Christian Mayr, Ryad Benosman, et al. Neuromorphic computing at scale. *Nature*, 637(8047):801–812, 2025.
- [10] Doo Seok Jeong and Cheol Seong Hwang. Nonvolatile memory materials for neuromorphic intelligent machines. *Advanced Materials*, 30(42):1704729, 2018.
- [11] Thomas L Carroll. Optimizing reservoir computers for signal classification. *Frontiers in Physiology*, 12:685121, 2021.
- [12] R Stanley Williams. How we found the missing memristor. *IEEE Spectrum*, 45(12):28–35, 2008.
- [13] Rivu Midya, Zhongrui Wang, Saumil Asapu, Xuanyao Zhang, Miao Rao, Wenhao Song, Yuhao Zhuo, Nishant Upadhyay, Qiangfei Xia, and J Joshua Yang. Reservoir computing using diffusive memristors. *Advanced Intelligent Systems*, 1(7):1900084, 2019.
- [14] Yinan Zhong, Jianshi Tang, Xinyi Li, et al. A memristor-based analogue reservoir computing system for real-time and power-efficient signal processing. *Nature Electronics*, 5:672–681, 2022.
- [15] Mario Lanza, Sebastian Pazos, Francisca Aguirre, Abu Sebastian, Manuel Le Gallo, Syed Minhaz Alam, Sadahiko Ikegawa, J Joshua Yang, Elisa Vianello, Meng-Fan Chang, et al. The growing memristor industry. *Nature*, 640(8059):613–622, 2025.
- [16] Mengru Jiang, Yujie Xu, Zhen Li, and Cheng Li. Current opinions on memristor-accelerated machine learning hardware. *Current Opinion in Solid State and Materials Science*, 37:101226, 2025.
- [17] Andreas Elschner, Sven Kirchmeyer, Werner Lovenich, Udo Merker, and Klaus Reuter. *PEDOT: Principles and Applications of an Intrinsically Conductive Polymer*. CRC Press, Boca Raton, FL, 2010.
- [18] Yoon Ho Jang, Wookyung Kim, Joon Kim, Kyung Seok Woo, Hye Jin Lee, Jong Won Jeon, Seung Kyun Shim, Jiyong Han, and Cheol Seong Hwang. Time-varying data processing with nonvolatile memristor-based temporal kernel. *Nature Communications*, 12(1):5727, 2021.
- [19] Mark A Lampert and Robert B Schilling. Current injection in solids: The regional approximation method. In *Semiconductors and Semimetals*, volume 6, pages 1–96. Elsevier, 1970.
- [20] Alexandre M Nardes, Martijn Kemerink, and René AJ Janssen. Anisotropic hopping conduction in spin-coated pedot: Pss thin films. *Physical Review B*, 76(8):085208, 2007.

- [21] Zhiyuan Zou, Aram Jang, Ethan T MacKnight, Po-Ming Wu, Junseok Do, Jae Sung Shim, Paul L Bishop, and Chong H Ahn. An on-site heavy metal analyzer with polymer lab-on-a-chips for continuous sampling and monitoring. *IEEE Sensors Journal*, 9(5):586–594, 2009.
- [22] Muhammad Hassan Mubarik, Dennis D Weller, Nathaniel Bleier, Matthew Tomei, Jasmin Aghassi-Hagmann, Mehdi B Tahoori, and Rakesh Kumar. Printed machine learning classifiers. In *2020 53rd Annual IEEE/ACM International Symposium on Microarchitecture (MICRO)*, pages 73–87. IEEE, 2020.
- [23] Mohammad Hossein Tayarani-Najaran and Michael Schmuker. Event-based sensing and signal processing in the visual, auditory, and olfactory domain: A review. *Frontiers in Neural Circuits*, 15:610446, 2021.
- [24] Jing Liu, Jingwei Zhang, and Yinghong Wang. Secure communication via chaotic synchronization based on reservoir computing. *IEEE Transactions on Neural Networks and Learning Systems*, 35(1):285–299, 2022.
- [25] Andrew Adamatzky, Phil Ayres, Alexander E Beasley, Alessandro Chiolerio, Mohammad M Dehshibi, Antoni Gandia, Elena Albergati, et al. Fungal electronics. *Biosystems*, 212:104588, 2022.
- [26] Andrew Adamatzky, Phil Ayres, Alexander E Beasley, Nic Roberts, and Han AB Wösten. Logics in fungal mycelium networks. *Logica Universalis*, 16(4):655–669, 2022.
- [27] Nic Roberts and Andrew Adamatzky. Mining logical circuits in fungi. *Scientific Reports*, 12(1):15930, 2022.
- [28] Alexander E Beasley, Anna L Powell, and Andrew Adamatzky. Capacitive storage in mycelium substrate. *arXiv preprint arXiv:2003.07816*, 2020.
- [29] Konrad Szaciłowski, Alexander E Beasley, Krzysztof Mech, and Andrew Adamatzky. Fungal capacitors. In *Fungal Machines: Sensing and Computing with Fungi*, pages 177–192. Springer, 2023.
- [30] Alexander E Beasley, Michail-Antisthenis Tsompanas, and Andrew Adamatzky. Fungal photosensors. In *Fungal Machines: Sensing and Computing with Fungi*, pages 123–130. Springer, 2023.
- [31] Doris Danninger, Robert Pruckner, Lisa Holzinger, Reinhard Koeppe, and Martin Kaltenbrunner. Myceliotronics: Fungal mycelium skin for sustainable electronics. *Science Advances*, 8(45):eadd7118, 2022.
- [32] Luke Heaton, Boguslaw Obara, Vicente Grau, Nick Jones, Toshiyuki Nakagaki, Lynne Boddy, and Mark D Fricker. Analysis of fungal networks. *Fungal Biology Reviews*, 26(1):12–29, 2012.
- [33] Zhongbiao Lu, Zhenzhen Chen, Yang Liu, Xiaomei Hua, Chunxiang Gao, and Jie Liu. Morphological engineering of filamentous fungi: Research progress and perspectives. *Journal of Microbiology and Biotechnology*, 34(6):1197, 2024.
- [34] Sophie Vandelook, Elise Elsacker, Aurélie Van Wylick, Lars De Laet, and Eveline Peeters. Current state and future prospects of pure mycelium materials. *Fungal Biology and Biotechnology*, 8(1):20, 2021.
- [35] Alison T Snyder, Jake M Winiski, and Eben D Bayer. Methods for controlling geometric regularity and homogeneity of aerial mycelium topologies and products of aerial mycelium with geometrically regular or homogeneous topologies, 2023. U.S. Patent Application 18/181,497.
- [36] Jake M Winiski, Gavin R McIntyre, Andrew J Carlton, and Joseph A Bevevino. Methods for controlling geometric regularity and homogeneity of aerial mycelium topologies and products of aerial mycelium with geometrically regular or homogeneous topologies, 2025. U.S. Patent Application 18/826,794.
- [37] Laura Greetham, Gavin R McIntyre, Eben Bayer, Jake Winiski, and Stephen Araldi. Mycological biopolymers grown in void space tooling, 2022. U.S. Patent 11,277,979.
- [38] Johannes Schindelin, Ignacio Arganda-Carreras, Erwin Frise, Verena Kaynig, Mark Longair, Tobias Pietzsch, Stephan Preibisch, Curtis Rueden, Stephan Saalfeld, Benjamin Schmid, et al. Fiji: an open-source platform for biological-image analysis. *Nature Methods*, 9(7):676–682, 2012.
- [39] Oscar Lee, Tianyi Wei, Kilian D Stenning, Jack C Gartside, Dan Prestwood, Shinichiro Seki, Aisha Aqeel, Kosuke Karube, Naoya Kanazawa, Yasujiro Taguchi, et al. Task-adaptive physical reservoir computing. *Nature Materials*, 23(1):79–87, 2024.
- [40] Martin Freiberger, Peter Bienstman, and Joni Dambre. A training algorithm for networks of high-variability reservoirs. *Scientific Reports*, 10(1):14451, 2020.
- [41] Norman P Jouppi, Cliff Young, Nishant Patil, David Patterson, Gaurav Agrawal, Raminder Bajwa, Sarah Bates, Suresh Bhatia, Nan Boden, Al Borchers, et al. In-datacenter performance analysis of a tensor processing unit. In *Proceedings of the 44th Annual International Symposium on Computer Architecture*, pages 1–12, 2017.
- [42] Ian E Jacobs and Adam J Moulé. Controlling molecular doping in organic semiconductors. *Advanced Materials*, 29(42):1703063, 2017.

- [43] Zhiyuan Xia, Xin Sun, Zeyang Wang, Jialin Meng, Bangfu Jin, and Ting Wang. Low-power memristor for neuromorphic computing: From materials to applications. *Nano-Micro Letters*, 17(1):217, 2025.
- [44] Ankur Singh, Suyoun Choi, Geng Wang, Malay Daimari, and Byung Gook Lee. Analysis and fully memristor-based reservoir computing for temporal data classification. *Neural Networks*, 182:106925, 2025.
- [45] Dongliang Wang, Yujie Nie, Gaolei Hu, Hon Ki Tsang, and Chaoran Huang. Ultrafast silicon photonic reservoir computing engine delivering over 200 tops. *Nature Communications*, 15(1):10841, 2024.
- [46] Martin AA Fiers, Thomas Van Vaerenbergh, Francis Wyffels, David Verstraeten, Benjamin Schrauwen, Joni Dambre, and Peter Bienstman. Nanophotonic reservoir computing with photonic crystal cavities to generate periodic patterns. *IEEE Transactions on Neural Networks and Learning Systems*, 25(2):344–355, 2013.
- [47] Daiki Nishioka, Tohru Tsuchiya, Masataka Imura, Yasuo Koide, Takashi Higuchi, and Kazuya Terabe. A high-performance deep reservoir computer experimentally demonstrated with ion-gating reservoirs. *Communications Engineering*, 3(1):81, 2024.
- [48] Wataru Namiki, Daiki Nishioka, Yusuke Yamaguchi, Tohru Tsuchiya, Takashi Higuchi, and Kazuya Terabe. Experimental demonstration of high-performance physical reservoir computing with nonlinear interfered spin wave multidetection. *Advanced Intelligent Systems*, 5(12):2300228, 2023.
- [49] Theofilos P Chatzinikolaou, Anastasios Mavropoulis, Ioannis Tompris, Georgios Kleitsiotis, Ioannis K Chatzipaschalidis, Konstantinos A Tsakalos, Iosif-Angelos Fyrigos, Michail-Antisthenis Tsompanas, Andrew Adamatzky, Panagiotis Dimitrakis, et al. Enabling mycelium-inspired reservoir computing with memristive oscillating cellular automata. In *2025 IEEE International Symposium on Circuits and Systems (ISCAS)*, pages 1–5. IEEE, 2025.
- [50] Luca Iannello, Lorenzo Ciampi, Giuseppe Lagani, Fabrizio Tonelli, Ezio Crocco, Luca Matteo Calcagnile, Angelo Di Garbo, Federico Cremisi, and Giuseppe Amato. From neurons to computation: biological reservoir computing for pattern recognition. *arXiv preprint arXiv:2505.03510*, 2025.
- [51] Xin Liu and Keshab K Parhi. Dna memristors and their application to reservoir computing. *ACS Synthetic Biology*, 11(6):2202–2213, 2022.
- [52] Haoyu Zhang and Danilo Vasconcellos Vargas. A survey on reservoir computing and its interdisciplinary applications beyond traditional machine learning. *IEEE Access*, 11:81033–81070, 2023.
- [53] J Buth. The mushroom industry in the netherlands. In Diego Cunha Zied and Arturo Pardo-Giménez, editors, *Edible and Medicinal Mushrooms: Technology and Applications*, pages 197–209. Wiley, 2017.
- [54] G. Bradski. The opencv library. *Dr Dobb's Journal – Software Tools for the Professional Programmer*, 25:120–125, November 2000.
- [55] P. Virtanen, R. Gommers, T.E. Oliphant, M. Haberland, T. Reddy, D. Cournapeau, and et al. Scipy 1.0: Fundamental algorithms for scientific computing in python. *Nature Methods*, 17(3):261–272, March 2020.
- [56] P.A.P. Moran. Notes on continuous stochastic phenomena. *Biometrika*, 37(1–2):17–23, 1950.
- [57] A.D. Cliff and J.K. Ord. *Spatial Autocorrelation*. Pion, London, 1973.
- [58] M. Abadi, P. Barham, J. Chen, Z. Chen, A. Davis, J. Dean, and et al. Tensorflow: A system for large-scale machine learning. In *Proceedings of the 12th USENIX Symposium on Operating Systems Design and Implementation (OSDI '16)*, pages 265–283, Savannah, GA, USA, November 2016.
- [59] D.P. Kingma and J. Ba. Adam: A method for stochastic optimization. In Y. Bengio and Y. LeCun, editors, *Proceedings of the 3rd International Conference on Learning Representations*, San Diego, CA, 2015. Published as arXiv preprint 1412.6980 in Dec 2014.
- [60] N. Srivastava, G. Hinton, A. Krizhevsky, I. Sutskever, and R. Salakhutdinov. Dropout: A simple way to prevent neural networks from overfitting. *Journal of Machine Learning Research*, 15(56):1929–1958, 2014.
- [61] M. Stone. Cross-validatory choice and assessment of statistical predictions (with discussion). *Journal of the Royal Statistical Society: Series B (Methodological)*, 36(2):111–147, 1974.
- [62] S.M. Lundberg and S.I. Lee. A unified approach to interpreting model predictions. In *Proceedings of Neural Information Processing Systems (NeurIPS)*, pages 4768–4777, Long Beach, CA, USA, 2017.
- [63] M.T. Ribeiro, S. Singh, and C. Guestrin. "why should i trust you?": Explaining the predictions of any classifier. In *Proceedings of the 22nd ACM SIGKDD International Conference on Knowledge Discovery and Data Mining (KDD '16)*, pages 1–10, San Francisco, CA, USA, 2016.
- [64] H. Hotelling. Analysis of a complex of statistical variables into principal components. *Journal of Educational Psychology*, 24:417–441, 1933.

- [65] S.P. Lloyd. Least squares quantization in pcm. *IEEE Transactions on Information Theory*, 28(2):129–137, 1982.
- [66] P. Thévenaz, U.E. Ruttimann, and M. Unser. A pyramid approach to subpixel registration based on intensity. *IEEE Transactions on Image Processing*, 7(1):27–41, January 1998.
- [67] F. Pedregosa, G. Varoquaux, A. Gramfort, V. Michel, B. Thirion, O. Grisel, and et al. Scikit-learn: Machine learning in python. *Journal of Machine Learning Research*, 12:2825–2830, October 2011.
- [68] C.E. Shannon. A mathematical theory of communication. *Bell System Technical Journal*, 27(3):379–423, 1948.
- [69] A. Kraskov, H. Stögbauer, and P. Grassberger. Estimating mutual information. *Physical Review E*, 69(6):066138, June 2004.

## S1 Supplementary Information

### S1.1 Mycelium Chip Specimen Imaging and Morphological Featurization

All 50x100x1mm mycelium specimens were imaged via transmitted light using the film scanning function of an Epson V600 scanner, with image capture performed both before and after PEDOT:PSS infusion. Morphological analysis of transmitted light images was performed using a custom image processing pipeline implemented in Python, with OpenCV [54], and SciPy [55]. High-resolution images of each specimen were converted to grayscale, contrast-enhanced, and smoothed using Gaussian blur to optimize feature visibility. Blob detection was applied using parameterized filtering on area, circularity, convexity, and inertia, enabling quantification of individual morphological units. For each blob, diameter, area, and mean grayscale intensity were extracted, and summary statistics (mean, standard deviation, minimum, maximum, and median) were calculated. Additionally, whole-image texture features were computed from the grayscale histogram, including contrast, energy, homogeneity, entropy, variance, skewness, kurtosis, autocorrelation, and difference entropy. The resulting feature set captured both local (blob-level) and global (image-level) structural characteristics for downstream dimension reduction and morphological-electrical property analyses.

### S1.2 Mycelium Chip Electrical Characterization

For each specimen we measured resistance, capacitance and voltage-current (V-I) curves. Resistance across the specimen was measured in a matrix pattern Keithley 2400 source meter using 4-wire Keithley 5805 Kelvin probes at 2V, 16V and 18V reference voltages. Similarly, capacitance was measured using the ET4410 LCR meter also at the same locations with a sign wave signal (Frequency @ 1kHz, Input Impedance @ 100 Ohms, Voltage @ 1V peak-to-peak). Voltage-current (IV) response was measured using Keithley 2400 source meter with a full voltage sweep (1-20V, with .5V step increments) (Figure S1). Tests were repeated twice for each specimen to validate findings. We consistently found a non-linear relationship in all specimens.

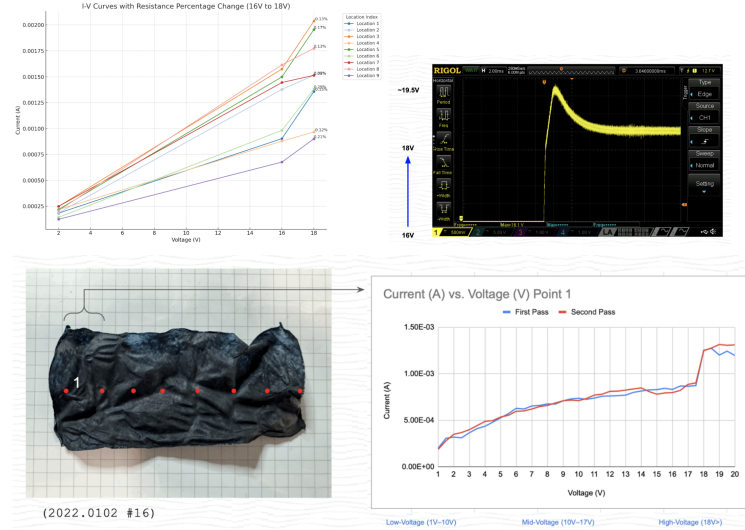


Figure S1: Electrical characterization of mycelium specimens shows consistent non-linear I-V behavior across all samples, measured via resistance, capacitance, and voltage sweeps.

Morphology influences PEDOT absorption and causes non-linearity in conductivity. We leverage the electrical differences exhibited at the different parts of the chip to model an electrical reservoir network for computation. We defined reservoirs as electrically addressable areas, or regions of interest (ROI), on the mycelium chip in which current can be passed and read through two pins. As electricity goes through the hyphal network there is a non-linear voltage drop across the pins, which can be attributed to the variable

We observed that hyphal structures exhibited a non-linear (diode-like) behavior between 16-18V on all tested locations on the surface. Mapping all different locations' response rate allowed us to map a dynamic reservoir network that can exhibit a delay (memory effect). We attributed this critical transition point as space-charge limited conduction (SCLC) in which the traps within the hyphal networks fill in and cause increased current flow.

To be able to commission a chip, we ran a calibration process to evaluate the electrical response of mycelium at 8 locations. We passed a 0-20V test signal through gold plated prongs (spaced 3mm apart) arranged in a matrix to measure the voltage and its decay time.

### S1.3 Global Electrical Resistance of Mycelium Chips as a Combined Function of PEDOT:PSS Uptake and Mycelium Morphological Qualities

Mycelium chip specimens were selected to represent a cross-section of morphological variance reflecting a subset of the total ‘morphological vocabulary’ that is addressable through tuning aerial mycelium growth parameters. Figure S2 shows the transmitted light image of each included specimen annotated with its respective characterized electrical resistance after PEDOT:PSS infusion.

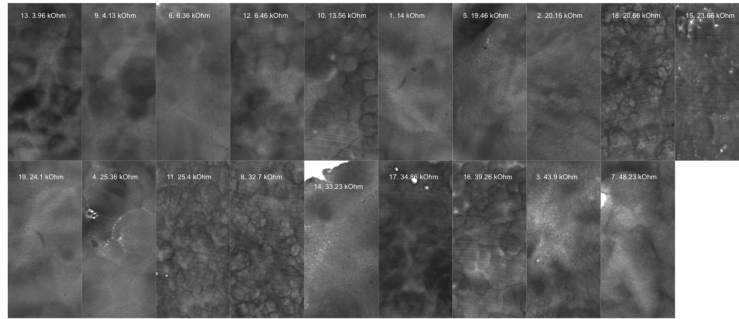


Figure S2: PEDOT:PSS infused mycelium morphologies characterized with lightbox imaging and resistive measurements.

First, the relationship between absolute uptake mass of PEDOT:PSS and electrical resistance was evaluated. It was found that there was a significant ( $p=0.5-0.004$ ) negative linear relationship between absolute uptake mass of PEDOT:PSS and resistance at all test positions, but with low correlation ( $R^2=.2-.41$ ). Fig S3 shows the linear correlation between absolute PEDOT:PSS uptake mass and measured resistance at each of four test positions.

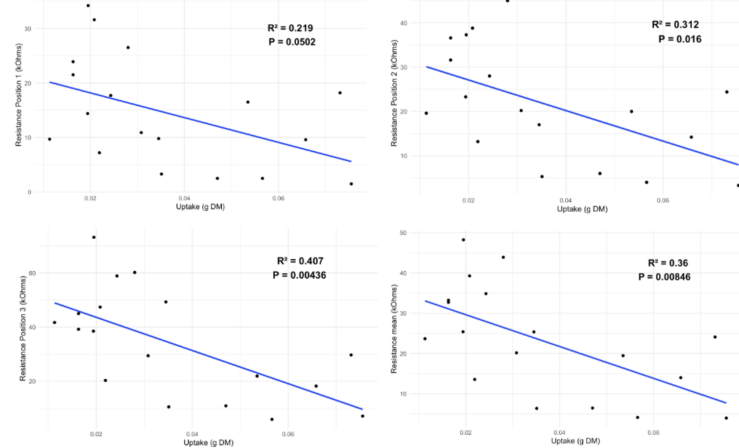


Figure S3: Correlation between absolute PEDO:PSS uptake and resistance.

This observed negative linear relationship between electrical resistance and absolute mass uptake of PEDOT:PSS is consistent with the role of PEDOT:PSS as a conductive dopant that enhances charge transport within the mycelium matrix. As the amount of infused PEDOT:PSS increases, a greater number of conductive pathways are formed, reducing the overall resistivity of the composite material.

Further evaluation of the relationship between mycelium mat morphology and residual resistance not explained by PEDOT:PSS mass uptake was performed (Figure S4). Dimension reduction of the resultant total morphological feature space was performed via principal component analysis, then spatial autocorrelation of residual resistance within the k-dimensional morphological space was used to evaluate the degree of organization of electrical resistance according to morphology.

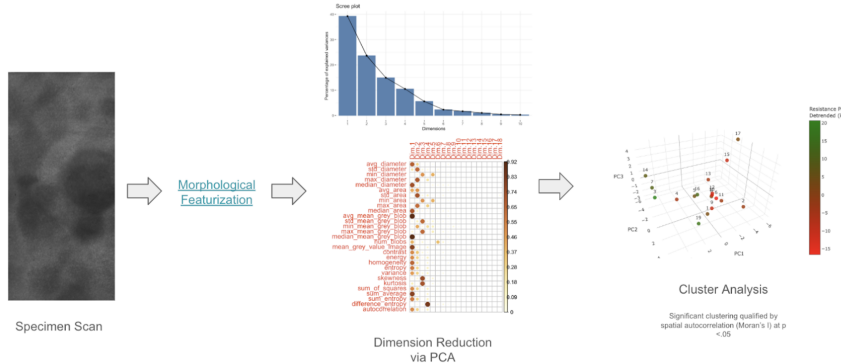


Figure S4: Specimen morphology analysis workflow.

Our cluster shows residual resistance (at measurement position 1) within the k-dimensional morphological space defined by principal components 1, 2, and 3 (representing >70% of total morphological variance). In this case a Moran's I p-value of .003 provides evidence of significant organization of residual resistance variance within the morphological feature space [56, 57]. Further testing of residual resistance at test positions 2 and 3 also supports evidence of significant autocorrelation within the morphological feature space ( $p=.007$  and  $.005$ , respectively).

To further evaluate the relative importance of morphology for explaining resistance independent of tissue density and PEDOT:PSS uptake, feature importance was performed by:

1. Training a regression neural network (TensorFlow)[58, 59, 60, 61] that attempts to explain mean resistance of all four test positions as a combined function of pre-infusion specimen density, the absolute mass uptake of PEDOT:PSS, the uptake rate of PEDOT:PSS (g uptake per g tissue mass), and morphology (represented by principal components 1-4, capturing >80% of total morphological variance).
2. Reasonable predictive quality was resolved (coefficient-of-determination = 0.54), so feature importance was performed via SHAP (SHapley Additive exPlanations)[62] to evaluate the relative importance of morphology for explaining resistance, then,
3. LIME (Local Interpretable Model-agnostic Explanations) was used to explore what characteristics best explain the lowest and highest resistance specimens in the sample set [63].

The plot in Figure S5 shows the results of SHAP analysis showing the relative importance of each feature for explaining mean resistance (from top to bottom). Morphological PC1 demonstrated the strongest explanatory power for mean resistance followed by absolute mass uptake of PEDOT:PSS and morphological PC3 and PC4. This would suggest morphology is strongly related to resistance in combination with PEDOT mass uptake. Lower explanatory power is also associated with tissue density independent of morphology and the uptake rate of PEDOT, followed by morphological PC2. Generally, this suggests morphology is potentially impactful on resistance performance independent of (1) mass uptake of PEDOT:PSS and (2) tissue density. Further, there is sensitivity to multiple independent dimensions of morphology, potentially suggesting more complex relationships.

Furthermore, the results of LIME analysis suggest which features are most critical for explaining the lowest (specimen 13) and highest (specimen 7) resistance (Figure S6). The results suggest attaining a low resistance is dependent on first attaining a high PEDOT:PSS uptake mass, then a particular morphology, followed by a high tissue density. Alternatively, attaining a high resistance is first dependent on morphology then a reduced PEDOT:PSS uptake mass.

To further explore discrete relationships between morphology and resistance, model training and feature importance was performed again with the original morphological feature set (Figure S7). A model was resolved with a coefficient-of-determination of  $R^2=0.43$ , from which below shows the results of feature importance ranking via SHAP analysis displaying the top 12 features based on magnitude of impact on mean resistance.

The top two ranked features for predicting mean resistance are the number of discrete blobs detected in the image and the absolute mass of PEDOT:PSS taken up by the specimen. 'num\_blobs' is the number of detected blobs, representing the density of distinct features or objects in the image and can indicate fragmentation, clustering, or structural complexity. This would suggest that the combination of complexity with uptake mass of PEDOT:PSS is impactful to resistance, with high resistance associated with increased complexity and reduced uptake.

Additional features (in descending importance) are:

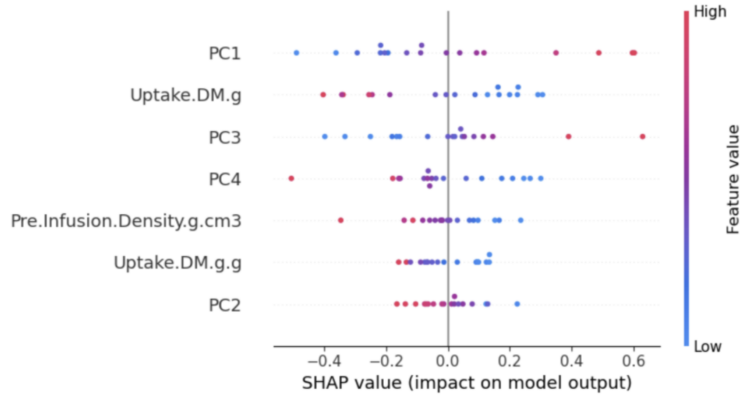


Figure S5: SHAP analysis reveals that morphological complexity, particularly PC1, is the strongest predictor of mycelium chip resistance, exceeding the influence of PEDOT:PSS uptake and tissue density.

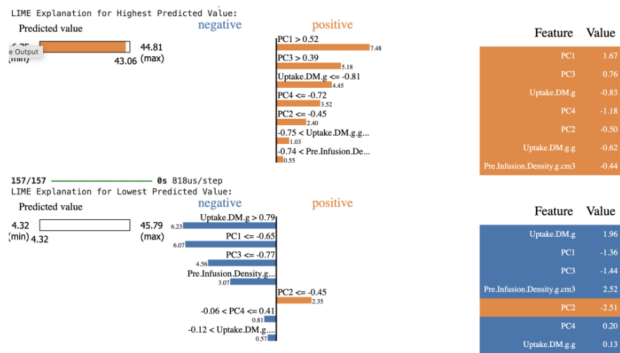


Figure S6: LIME analysis identifies PEDOT:PSS uptake as the primary driver of low resistance and morphology as the dominant factor in high resistance across mycelium chip specimens.

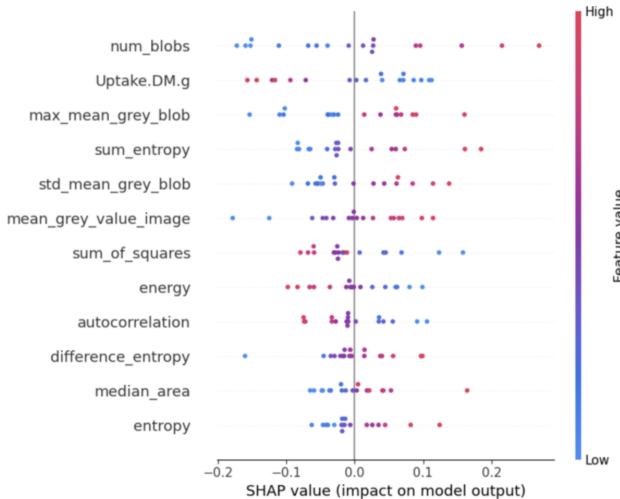


Figure S7: SHAP analysis ranks the top 12 morphological features impacting mean resistance, led by structural complexity and PEDOT:PSS uptake.

1. Maximum mean grey value, or the within-blob maximum tissue density.
2. Textural complexity 'sum\_entropy', with high textural complexity associated with increased resistance.
3. Within-blob mean grey value variance, indicating high tissue density variance within blobs as associated with increased resistance.
4. The global mean grey value of the specimen.
5. Image texture as sum of squares, where low values would indicate more homogeneous or smooth textures.
6. Texture uniformity as energy, where low values would indicate complex textures.
7. Autocorrelation indicating the degree of repetitive patterns or spatial similarity, with low values indicating more random and irregular textures.
8. Texture as difference entropy, with high values indicating greater texture complexity.
9. The median size of detected blobs, indicating greater resistance with larger blob sizes.
10. Texture complexity as entropy, where high values are associated with increased texture complexity.

In total, the feature importance narrative suggests that morphological complexity is highly consequential to ultimate resistance in combination with the absolute mass of PEDOT:PSS taken up by the specimen and density of the specimen. In this case it is suggested that as morphological complexity increases resistance increases independent of the absolute amount of PEDOT:PSS infused. Given this, it may be suggested that a range of resistance or electrical responsiveness may be accessed as a function of morphology given the wide range of morphological complexity and variation addressable in aerial mycelium.

#### **S1.4 Classification of Local Electrical Properties of Mycelium Chip Specimens as a Function of Global and Local Morphological Qualities**

To identify meaningfully distinct mycelium morphologies for characterization, the source aerial mycelium sample population was processed with the morphological featurization pipeline and discretized using Principal Component Analysis (PCA) and k-means clustering [64, 65]. K-means clustering was employed to identify patterns in the extracted image features by partitioning the data into K distinct clusters based on similarity. Prior to clustering, features were standardized using z-score normalization to ensure equal weighting. The optimal number of clusters was selected via the elbow method, which evaluates the within-cluster sum of squares (WCSS) across increasing values of K. PCA was applied for dimensionality reduction and visualization of the clustering results. Clusters were selected by first identifying the pair of clusters with the greatest Euclidean distance between their centroids, representing the most dissimilar pair. A third cluster was then chosen by maximizing the combined distance from both of the initially selected clusters, ensuring maximal overall diversity among the three selected clusters. The below plot shows morphologically distinct cluster groups within the k-dimensional space (PC1 and PC2), where specimens from clusters 0, 2, and 3 were selected for subsequent characterization in order to maximize morphological variety (Figure S8).

We were able to cluster the original mycelium mat sample sets discretized into morphologically related cluster groups 0, 2, and 3 per the above k-means cluster analysis (Figure S9).

Finally, mycelium chip specimens were prepared from one representative mycelium mat specimen from each of the selected morphological groups (Figure S10). Specimens were prepared in acrylic templates such that local electrical and morphological properties could be evaluated at up to 10 discrete positions. The below image shows the prepared 100x50x1mm specimens from each of classes 0, 2, and 3 before and after PEDOT:PSS infusion.

Local electrical properties were characterized according to the sample positions defined by the acrylic template. Mycelium chip specimens were imaged before and after PEDOT:PSS infusion, images cropped to their respective final dimensions, and pre- and post-infusion images aligned using a rigid body alignment in FIJI [38, 66]. Regions of interest (ROI) were defined based on the acrylic sampling template in the post-infusion image, then each ROI measured from the pre-infusion specimen in order to correlate local post-infusion electrical properties to pre-infusion tissue morphology. For each ROI the grey value distribution and summary statistics were measured in FIJI. Histogram-based image features were extracted from the greyscale intensity distributions by computing statistical (mean, variance, skewness, kurtosis), shape (entropy, energy, contrast, homogeneity), and cumulative (interquartile range) descriptors. Additionally, whole chip specimen morphological featurization was performed as previously and dimension reduced via PCA to provide global morphological features. Resistance and conductivity data from electrical characterization were aggregated and the IV curves featurized by fitting linear regression models for each ROI, extracting parameters including slope, intercept, R<sup>2</sup>, p-value, and residual statistics. Finally, electrical target distributions were evaluated and appropriate transformations (boxcox or log) applied to manage outliers and skewness prior to model training. This resulted in a data set from which local electrical properties after PEDOT:PSS infusion could be evaluated as a combined function of

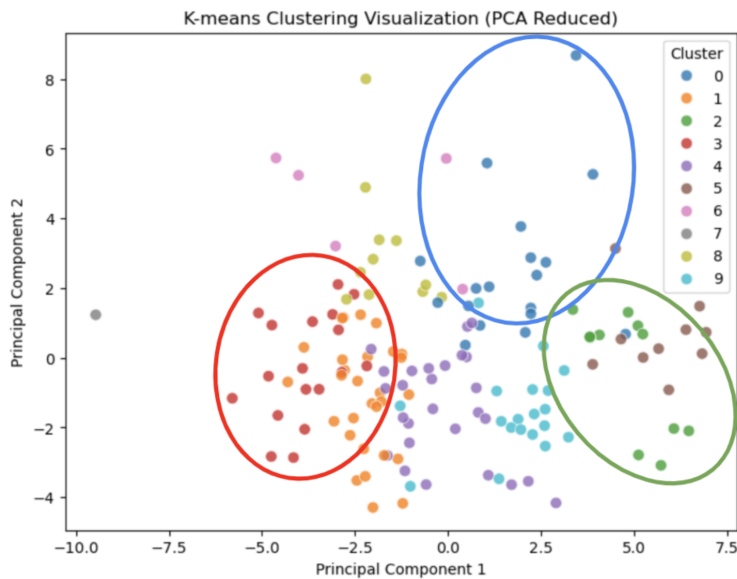


Figure S8: PCA and k-means clustering of morphological features identify three maximally distinct mycelium specimen groups selected for downstream electrical characterization.

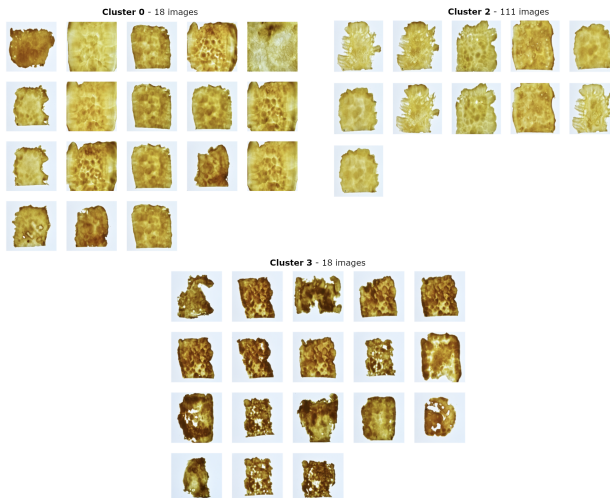


Figure S9: Mycelium samples clustered into groups 0, 2, and 3 based on morphological similarity.

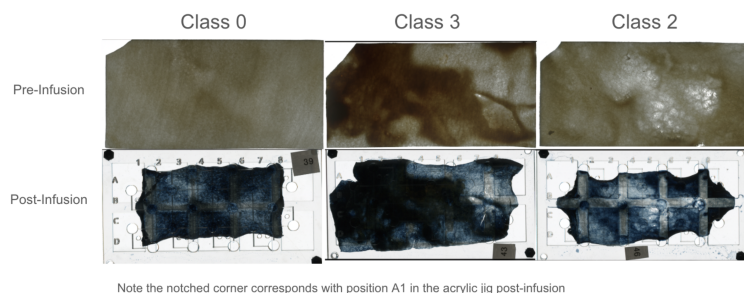


Figure S10: Representative mycelium chip specimens from clusters 0, 2, and 3 before and after PEDOT:PSS infusion, prepared for localized electrical and morphological analysis.

global and local mycelium morphology prior to infusion. Subsequent analysis evaluated the potential for explaining post-infusion local electrical properties based on pre-infusion morphology.

Figure S11 illustrates ROI alignment to pre- and post-PEDOT:PSS infused specimens (morphological class 0), as well as characterized current (2V) and I-V non-linearity (sum of squared residuals).

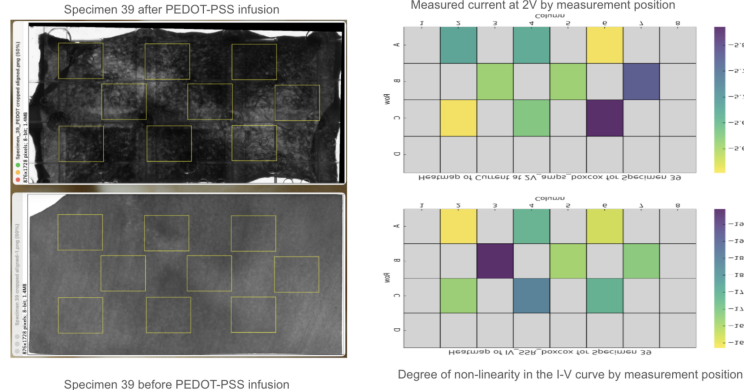


Figure S11: ROI alignment on pre- and post-infusion specimens (class 0), with mapped current (2V) and I-V non-linearity illustrating spatial variation in electrical response.

PCA was performed on the target space (combination of all conductance, resistance, and I-V features) to determine the degree of co-variability. The results suggest that all measured electrical features are highly correlated with one another, collapsing the whole electrical response space to a single response ('PC1', explaining >90% of total electrical variance) (Figure S12).

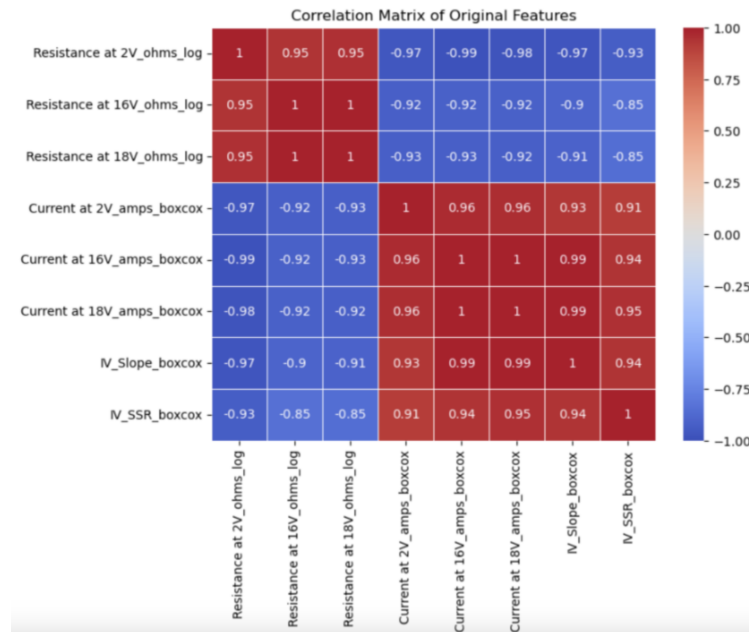


Figure S12: PCA of electrical features shows strong covariability, with PC1 capturing over 90% of total variance across conductance, resistance, and I-V metrics.

Mutual information analysis was performed to quantify the dependency between each of 17 features and multiple target variables using the 'mutual\_info\_regression' function from Scikit-learn[67, 68, 69]. For each target, mutual information scores were computed, stored, and visualized to highlight the most informative features. The results help identify which features share the most information with each target, where higher scores suggest a stronger

relationship. An aggregated average score across all targets was used to assess overall feature relevance. The results suggest that features are not noise-dominated and that the feature space holds predictive value for the electrical property target variable (Figure S13). Suggested feature importance in descending order is (1) global morphology (density and complexity), (2) local tissue density, (3) local tissue complexity/uniformity and eccentricity.

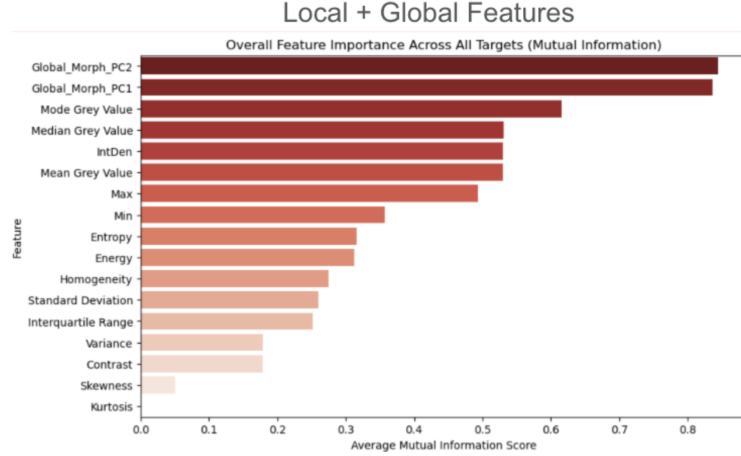


Figure S13: Mutual information analysis identifies global morphology, local density, and texture complexity as top predictors of electrical properties.

A regression neural network was trained to predict electrical property PC1 as a combined function of both global and local morphological features. A fully connected feedforward neural network was trained using leave-one-out cross-validation (LOOCV) to predict the electrical property (PC1) target from the feature set. The model architecture consisted of two hidden layers with 128 and 64 ReLU-activated units, respectively, incorporating L2 regularization and dropout to mitigate overfitting. Model performance was evaluated by aggregating prediction error and loss across all LOOCV folds, with mean squared error as the loss function and the Adam optimizer used for training.

A coefficient-of-determination of 0.74 was achieved, suggesting strong predictive utility for endpoint electrical properties as a function of original tissue morphology, allowing for classification of probable local electrical properties across an arbitrary morphological surface prior to physical infusion with PEDOT:PSS.

The results suggest that electrical performance of PEDOT:PSS infused mycelium chips have a significant relationship with morphological variation within the feedstock mycelium mat prior to PEDOT:PSS infusion. Further, the distribution of local electrical properties over a given mycelium mat area may be classified prior to infusion with PEDOT:PSS. The ability to pre-classify the distribution of electrical properties across a mycelium sheet prior to PEDOT:PSS infusion offers a powerful means of functionally screening and selecting material regions with desirable electrical behavior for reservoir computing depending on use case and application. By predicting properties such as resistance and I-V non-linearity based on native morphological features, this approach enables targeted use or exclusion of specific regions, optimizing the functional capacity and consistency of the reservoir. This pre-infusion classification may reduce empirical trial-and-error in reservoir training and support rational design of mycelium-based computational substrates through targeted morphological engineering during growth.

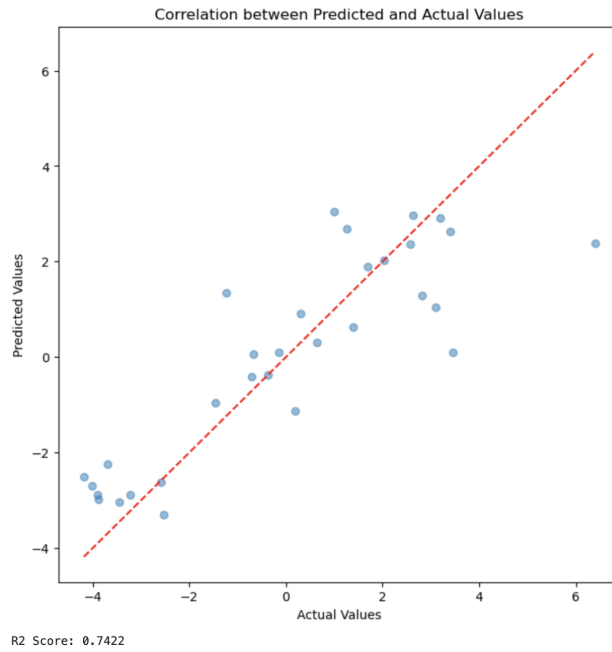


Figure S14: Mutual information analysis identifies global morphology, local density, and texture complexity as top predictors of electrical properties.

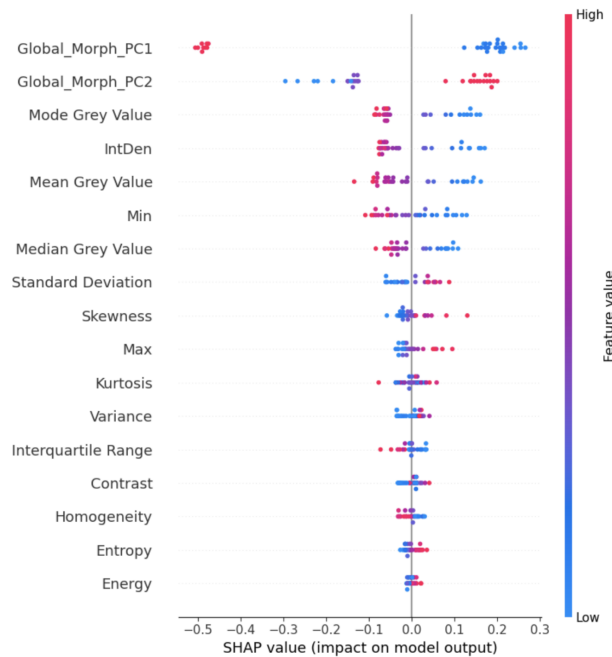


Figure S15: SHAP analysis ranking feature importance for electrical property response PC1 values.